A Comparative Study of Grid-Following and Grid-Forming Control Schemes in Power Electronic-Based Power Systems

Gao, Xian; Zhou, Dao; Anvari-Moghaddam, Amjad; Blaabjerg, Frede

Published in:
Power Electronics and Drives

DOI (link to publication from Publisher):
10.2478/pead-2023-0001

Publication date:
2023

Document Version
Publisher's PDF, also known as Version of record

Power Electronics and Drives
Volume 8(43), 2023 DOI: 10.2478/pead-2023-0001

sciendo

Power Electronics and Drives

A Comparative Study of Grid-Following and Grid-Forming Control Schemes in Power Electronic-Based Power Systems

Research paper

Xian Gao*, Dao Zhou, Amjad Anvari-Moghaddam, Frede Blaabjerg

AAU Energy, Aalborg University, Aalborg, Denmark

Received: 31, October 2022; Accepted: 30, November 2022

Abstract: Along with de-carbonisation, the penetration of power electronic converters has increased, and the power system has become a power electronic-based power system. In such a situation, the stability of the power system faces great challenges. In the event of a large disturbance, the power grid will lack the ability to maintain a stable voltage and frequency. In order to improve the stability of the power grid, the traditional grid-following (GFL) control is needed to be converted to the grid-forming (GFM) control. This paper analyses the control schemes of the GFL and GFM converters by investigating their state-space models, and the eigenvalue trajectories of both control schemes are shown to analyse the stability of the systems. Moreover, a case study is exemplified to compare the performance of the two control strategies while responding to frequency disturbances. Finally, a time-domain simulation model of a 15 kW grid-connected converter is built in Matlab/Simulink to benchmark the performance of the GFL and GFM converters under different working conditions. The result reveals that the GFL converter may encounter some instabilities when applied in power electronic-based systems, while the GFM converter is more suitable for the weak power grid.

Keywords: *grid-following control • grid-forming control • state-space model • stability analysis • grid strength*

1. Introduction

Global energy demand has been increasing over the past few decades. As a promising candidate, renewable energy is developing rapidly to cope with potential energy crises. Renewable energy systems will play an even more important role in future electricity production.

However, renewable energy resources are coupled to the power grid through power electronic converters, which respond quickly and do not provide any moment of inertia (Fang et al., 2018; Peng et al., 2019). Today's power grids rely on synchronous generators to generate mechanical inertia. These generators are very large and are synchronised with each other tightly, so small disturbances from the load or the generation process cannot influence the frequency stability of the power grid. However, distributed renewable energy systems are usually connected to the power grid using grid-following (GFL) converters instead of conventional synchronous generators. The goal of the GFL converter is to simply lock and track the grid frequency. GFL converters typically operate at their rated output power and do not respond to deviations in grid frequency as do synchronous generators (Lasseter et al., 2020). With the increasing popularity of renewable energy systems, many large central power plants are being phased out. Ultimately, the moment of inertia and damping of the entire grid to which the renewable energy system is connected are decreasing, resulting in a weaker ability of the grid to handle sudden deviations of the frequency. The characteristics of a low-inertia system have a great influence on the stability of the power grid. In order to improve the stability of a distributed power grid with highly penetrated renewable energy systems, the grid-forming (GFM) control strategy has emerged (Rocabert et al., 2012). One of the most popular

* Email: xiga@energy.aau.dk

GFM control strategies is the application of virtual synchronous generators (VSGs), which enables the converter to imitate the behaviour of conventional synchronous generators to improve the inertia and damping of the power grid (Chen et al., 2020).

This paper describes the above problems and discusses the performance of the GFL and GFM control systems under various working conditions. The main contributions of this paper can be summarised as follows. (1) Detailed illustrations of the typical structures of the GFL and GFM controls are given, and the state-space models of both the GFL and GFM controls are built. (2) A comparison between the GFL and GFM controls under various working conditions is done. (3) The simulation results show that the smaller the short circuit ratio (SCR) becomes, the greater is the impact that the load fluctuation has on the power grid and that the GFM control is more suitable for a weak power grid.

The remaining part of the paper is organised as follows. Section 2 describes the conceptual differences between the GFL and the GFM controls. In Sections 3 and 4, the control diagrams of the GFL and GFM controls are illustrated in detail and the state-space models of both the GFL and GFM controls are built. In Section 5, a simulation model of a grid-connected converter is built in Matlab/Simulink to compare the different performances of the GFL and GFM controls under various working conditions to verify the expected outcomes. Finally, some conclusions are drawn in Section 6.

2. Comparison Between the GFL Converter and the GFM Converter

Power converters can be divided into GFL converters and GFM converters according to their control schemes. The GFL converter can be simply represented as a controlled current source, as shown in Figure 1a, where Z_g is the equivalent grid impedance; $V_g\angle\delta_g$ is the grid voltage vector; $I_g\angle\varphi_g$ is the converter output currents. It usually uses a phase-locked loop (PLL) to track the phase angle of the voltages at the point of common coupling (PCC) to ensure that the converter is synchronised to the power grid (Wang et al., 2020). The GFL converter achieves the target injected active and reactive power by adjusting the currents injected into the power grid. However, it cannot provide regulation of the frequency and voltage for the grid directly, which acquires the frequency and voltage references from an additional voltage source or the power grid (Du et al., 2020). Therefore, the GFL converter cannot operate in an islanded mode and cannot handle the problems of frequency disturbances.

Instead, the GFM converter can be simply represented as a controlled voltage source, as shown in Figure 1b, where $E\angle\delta$ is the inverter ouput voltage vector. Some GFM control strategies do not require a PLL to track the phase angle of the voltages at the PCC and can imitate the conventional synchronous generators to achieve self-synchronisation with the power grid (Rosso et al., 2021). Compared to the conventional synchronous generators that provide frequency regulation by the stored rotating energy in the rotor, GFM converters can adjust their output faster to deal with frequency disturbances in the power grid (Pattabiraman et al., 2018). Therefore, the GFM converters are suitable for operation in an islanded mode.

In addition, some works in the literature demonstrate that the use of a PLL may affect the stable operation of the power converters in weak grids (Lasseter et al., 2020; Rosso et al., 2021). That is because the GFL converter tracks the voltages at the PCC, which is easily affected by the output currents in weak grids. On the contrary, the GFM

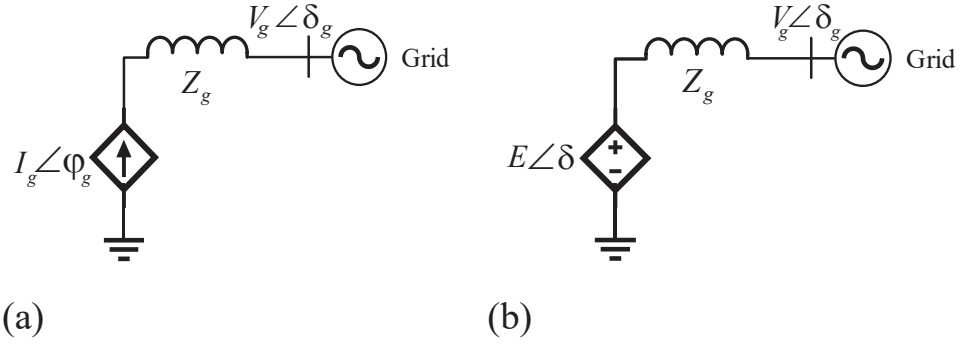

Fig. 1. Simplified representation of power converters: (a) GFL converter; (b) GFM converter. GFL, grid-following; GFM, grid-forming.

Control mode	Advantages	Disadvantages
GFL converter	1. Quick regulation 2. Simple control structure	1. Lack of frequency and voltage regulation 2. Unable to operate in an islanded mode 3. Instability in weak grids
GFM converter	1. Able to operate in an islanded mode 2. Provides the regulation of frequency and voltage	1. Instability in stiff grids 2. Easily susceptible to overload

GFL, grid-following; GFM, grid-forming.

Table 1. Comparison of GFL and GFM converters.

converter can achieve self-synchronisation based on the output active power, which allows it to synchronise to weak grids. However, in a stiff grid, a little phase difference between the converter voltages and grid voltages may lead to large fluctuations of active power, resulting in overload. Table 1 summarises the advantages and disadvantages of the GFL and GFM converters (Gao et al., 2021).

3. Control Structure of a GFL Converter

The GFL converter is widely used in distributed renewable energy systems. When grid-connected power converters are used as the interface between the renewable energy systems and power grids, most grid-connected converters with GFL control consist of a PLL unit and double-loop vector control. The GFL converter uses a PLL to track the phase angle of the voltages at the PCC and adopts a vector control strategy to adjust the active and reactive currents that are injected into the power grid. This paper adopts active - reactive power control (PQ control) as an outer control loop. For this control strategy, the outer loop is used to adjust the active and reactive power injected into the power grid, while the inner current is used to adjust the converter currents according to the reference values set by the outer power loop (Sangwongwanich et al., 2018).

The system topology of a GFL converter with the PQ control is shown in Figure 2, where u_{dc} is the DC-link voltage; u_a, u_b and u_c are the converter output voltages, respectively; i_a, i_b and i_c are the converter currents; u_{pcca}, u_{pccb} and u_{pccc} are the voltages at the PCC; u_{ga}, u_{gb} and u_{gc} are the grid voltages; i_{ga}, i_{gb} and i_{gc} are the grid currents; i_{Ca}, i_{Cb} and i_{Cc} are the capacitor currents; L_f and C_f are the inductance and capacitance, respectively, of the LC filter; L_g and R_g are the grid impedance and resistance, respectively; P_e and Q_e are the output active power and reactive power, respectively; P_{ref} and Q_{ref} are the references of active and reactive power, respectively.

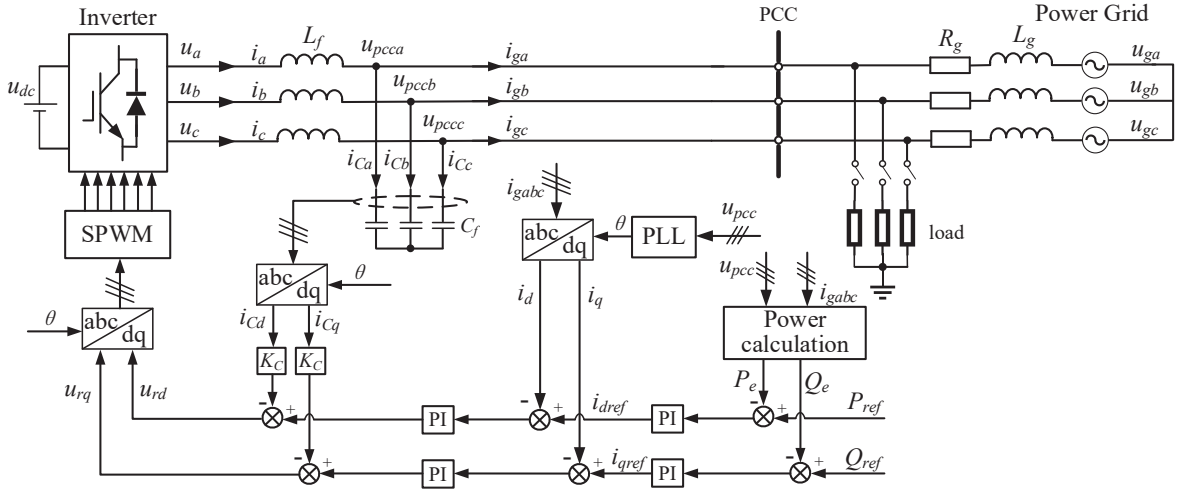

Fig. 2. The topology of a GFL converter with the PQ control. GFL, grid-following; PCC, point of common coupling; PI, proportional integral; PLL, phase-locked loop; SPWM, sinusoidal pulse width modulation.

3.1. The PLL unit

The PLL unit enables the converter to synchronise to the power grid. Because of the existence of the PLL, when small-signal perturbations are added, there is a small error $\theta_{pll} - \theta_s$ between the control synchronising frame (defined by the PLL) (Dong et al., 2015; Yang et al., 2019) and the actual system synchronising frame (defined by the PCC voltage). The actual system synchronising frame can be converted to the control synchronising frame using a rotation matrix T_θ:

$$T_\theta = \begin{bmatrix} \cos(\theta_{pll} - \theta_s) & \sin(\theta_{pll} - \theta_s) \\ -\sin(\theta_{pll} - \theta_s) & \cos(\theta_{pll} - \theta_s) \end{bmatrix} \approx \begin{bmatrix} 1 & \theta_{pll} - \theta_s \\ \theta_s - \theta_{pll} & 1 \end{bmatrix}. \tag{1}$$

The transformations between the two reference frames can be expressed as follows (Xie et al., 2019):

$$\begin{bmatrix} x_d^c \\ x_q^c \end{bmatrix} = T_{\Delta\theta} \begin{bmatrix} x_d^s \\ x_q^s \end{bmatrix} \approx \begin{bmatrix} 1 & \theta_{pll} - \theta_s \\ \theta_s - \theta_{pll} & 1 \end{bmatrix} \begin{bmatrix} x_d^s \\ x_q^s \end{bmatrix}; \tag{2}$$

$$\begin{bmatrix} x_d^s \\ x_q^s \end{bmatrix} = T_{\Delta\theta}{}^{-1} \begin{bmatrix} x_d^c \\ x_q^c \end{bmatrix} \approx \begin{bmatrix} 1 & \theta_s - \theta_{pll} \\ \theta_{pll} - \theta_s & 1 \end{bmatrix} \begin{bmatrix} x_d^c \\ x_q^c \end{bmatrix}, \tag{3}$$

where the subscripts *d* and *q* represent the *d*-axis and *q*-axis components of a variable; the variables in the actual system synchronising frame are marked with the superscript *s*, while the variables in the control synchronising frame are marked with the superscript *c*.

Adding small-signal perturbations to Eqs (2) and (3), they can be rewritten as follows:

$$\begin{bmatrix} X_{d0}^c + \Delta x_d^c \\ X_{q0}^c + \Delta x_q^c \end{bmatrix} = \begin{bmatrix} 1 & \theta_{pll} + \Delta\theta - \theta_s \\ \theta_s - (\theta_{pll} + \Delta\theta) & 1 \end{bmatrix} \begin{bmatrix} X_{d0}^s + \Delta x_d^s \\ X_{q0}^s + \Delta x_q^s \end{bmatrix}; \tag{4}$$

$$\begin{bmatrix} X_{d0}^s + \Delta x_d^s \\ X_{q0}^s + \Delta x_q^s \end{bmatrix} = \begin{bmatrix} 1 & \theta_s - (\theta_{pll} + \Delta\theta) \\ \theta_{pll} + \Delta\theta - \theta_s & 1 \end{bmatrix} \begin{bmatrix} X_{d0}^c + \Delta x_d^c \\ X_{q0}^c + \Delta x_q^c \end{bmatrix}, \tag{5}$$

where the subscript '0' denotes the steady-state values, and the prefix Δ denotes the small-signal disturbance of variables.

Because the control synchronising frame is aligned with the actual system synchronising frame in the steady state, it means that the angle error $\theta_{pll} - \theta_s$ is zero (Wen et al., 2016). Deleting the steady-state values, the linearised small-signal model of transformations can be given as follows:

$$\begin{bmatrix} \Delta x_d^c \\ \Delta x_q^c \end{bmatrix} = \begin{bmatrix} \Delta x_d^s \\ \Delta x_q^s \end{bmatrix} + \begin{bmatrix} X_{q0} \\ -X_{d0} \end{bmatrix} \cdot \Delta\theta; \tag{6}$$

$$\begin{bmatrix} \Delta x_d^s \\ \Delta x_q^s \end{bmatrix} = \begin{bmatrix} \Delta x_d^c \\ \Delta x_q^c \end{bmatrix} - \begin{bmatrix} X_{q0} \\ -X_{d0} \end{bmatrix} \cdot \Delta\theta. \tag{7}$$

The control scheme of the PLL is shown in Figure 3, where T_{PLL} is the proportional integral (PI) controller of the PLL; *s* is the Laplace variable. According to Figure 3, the relationship between $u_{\mathrm{pccq}}^{\mathrm{c}}$ and θ can be expressed as follows:

$$\theta_{PLL} = \frac{T_{PLL}(s)}{s} u_{pccq}^c = \left(k_{pPLL} + k_{iPLL} \frac{1}{s} \right) \frac{u_{pccq}^c}{s}, \tag{8}$$

where k_{pPLL} and k_{iPLL} are the proportional and integral parameters, respectively, for the PLL unit.

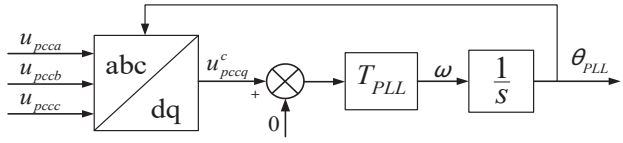

Fig. 3. Control scheme of the PLL. PLL, phase-locked loop.

The linearised small-signal model of the PLL unit can be derived as follows:

$$\Delta\theta = \frac{T_{PLL}(s)}{s}\Delta u^c_{pccq} = \left(k_{pPLL} + k_{iPLL}\frac{1}{s}\right)\frac{\Delta u^c_{pccq}}{s}. \tag{9}$$

According to Eqs (6) and (9), $\Delta\theta$ can be given as

$$\Delta\theta = \frac{T_{PLL}(s)}{s}\left(\Delta u^s_{pccq} - U_{pccd0}\Delta\theta\right). \tag{10}$$

In the time domain, Eq. (10) can be written as follows:

$$\frac{d\Delta\xi_q}{dt} = \Delta u^c_{pccq} = \Delta u^s_{pccq} - U_{pccd0}\Delta\theta; \tag{11}$$

$$\frac{d\Delta\theta}{dt} = k_{iPLL}\Delta\xi_q + k_{pPLL}\left(\Delta u^s_{pccq} - U_{pccd0}\Delta\theta\right). \tag{12}$$

Therefore, the state-space model of the PLL unit can be expressed as follows:

$$\Delta\dot{x}_{PLL} = A_{PLL}\Delta x_{PLL} + B_{PLL}\Delta x_{LCL}, \tag{13}$$

where

$$\Delta x_{PLL} = \begin{bmatrix}\Delta\xi_q & \Delta\theta\end{bmatrix}^T; \tag{14}$$

$$\Delta x_{LCL} = \begin{bmatrix}\Delta i^s_d & \Delta i^s_q & \Delta u^s_{pccd} & \Delta u^s_{pccq} & \Delta i^s_{gd} & \Delta i^s_{gq}\end{bmatrix}^T; \tag{15}$$

$$A_{PLL} = \begin{bmatrix}0 & -U_{pccd0}\\ k_{iPLL} & -k_{pPLL}U_{pccd0}\end{bmatrix}; \tag{16}$$

$$B_{PLL} = \begin{bmatrix}0 & 0 & 0 & 1 & 0 & 0\\ 0 & 0 & 0 & k_{pPLL} & 0 & 0\end{bmatrix}; \tag{17}$$

3.2. Power control loop

The outer power control loop is used to regulate the active and reactive power injected into the power grid. In the synchronous *d-q* reference frame, the instantaneous active and reactive power are decoupled and can be expressed as follows:

$$\begin{cases} p = \frac{3}{2}\left(u^c_{pccd}{i_{gd}}^c + u^c_{pccq}{i_{gq}}^c\right)\\ q = \frac{3}{2}\left(u^c_{pccq}{i_{gd}}^c - u^c_{pccd}{i_{gq}}^c\right)\end{cases}. \tag{18}$$

The average active and reactive power can be given as follows:

$$\begin{cases} P_e = \dfrac{\omega_c}{s+\omega_c} p \\ Q_e = \dfrac{\omega_c}{s+\omega_c} q \end{cases}, \tag{19}$$

where ω_c is the cut-off frequency of the low-pass filter (LPF) of the measured active and reactive power.

According to Eqs (18) and (19), the linearised small-signal equations can be expressed as

$$\Delta \dot{x}_{cal} = A_{cal}\Delta x_{cal} + B_{cal}\Delta x_{LCL}, \tag{20}$$

where

$$\Delta x_{cal} = \begin{bmatrix} \Delta P_e & \Delta Q_e \end{bmatrix}^T; \tag{21}$$

$$A_{cal} = \begin{bmatrix} -\omega_c & 0 \\ 0 & -\omega_c \end{bmatrix}; \tag{22}$$

$$B_{cal} = \begin{bmatrix} 0 & 0 & \dfrac{3}{2}\omega_c I_{gd0} & \dfrac{3}{2}\omega_c I_{gq0} & \dfrac{3}{2}\omega_c U_{pccd0} & \dfrac{3}{2}\omega_c U_{pccq0} \\ 0 & 0 & -\dfrac{3}{2}\omega_c I_{gq0} & \dfrac{3}{2}\omega_c I_{gd0} & \dfrac{3}{2}\omega_c U_{pccq0} & -\dfrac{3}{2}\omega_c U_{pccd0} \end{bmatrix}. \tag{23}$$

The outputs of the power loop serve as the references for the inner current loop. The outputs of the power loop can be given as follows:

$$\begin{cases} i_{dref}^c = \left(k_{pPQ} + k_{iPQ}/s\right)\left(P_{ref} - P_e\right) \\ i_{qref}^c = -\left(k_{pPQ} + k_{iPQ}/s\right)\left(Q_{ref} - Q_e\right) \end{cases}, \tag{24}$$

where k_{pPQ} and k_{iPQ} represent the proportional and integral coefficients, respectively, of the power control loop.

Two state-space variables γ_d and γ_q are introduced as shown below:

$$\begin{cases} \dfrac{d\gamma_d}{dt} = P_{ref} - P_e \\ \dfrac{d\gamma_d}{dt} = Q_{ref} - Q_e \end{cases}. \tag{25}$$

Combining Eqs (24) and (25), the linearised small-signal model can be given as follows:

$$\Delta \dot{x}_{PQ} = B_{PQ1}\Delta x_{cal}; \tag{26}$$

$$\Delta y_{PQ} = C_{PQ}\Delta x_{PQ} + D_{PQ}\Delta x_{cal}, \tag{27}$$

where

$$\Delta x_{PQ} = \begin{bmatrix} \Delta\gamma_d & \Delta\gamma_q \end{bmatrix}^T; \tag{28}$$

$$\Delta y_{PQ} = \begin{bmatrix} \Delta i_{dref}^c & \Delta i_{qref}^c \end{bmatrix}^T; \tag{29}$$

$$B_{PQ1}=\begin{bmatrix}-1 & 0\\ 0 & -1\end{bmatrix};\tag{30}$$

$$C_{PQ}=\begin{bmatrix}k_{iPQ} & 0\\ 0 & -k_{iPQ}\end{bmatrix};\tag{31}$$

$$D_{PQ}=\begin{bmatrix}-k_{pPQ} & 0\\ 0 & k_{pPQ}\end{bmatrix}.\tag{32}$$

3.3. Current loop

The inner current control loop is used to regulate the converter currents to follow the references set by the outer power loop and also to protect the power conversion. It is worthwhile to note that a virtual resistance-based active damping method is applied here to reduce the resonant peak without sacrificing the efficiency of the converter (Adapa and John, 2018; Dahono et al., 2001). The capacitor current is fed back into the current control loop. The outputs of the current control loop can be given as follows:

$$\begin{cases}u^c_{rdref}=\left(k_{pc}+k_{ic}/s\right)\left(i^c_{dref}-i^c_{gd}\right)-\omega_g L_g i^c_{gq}-K_C\left(i^c_d-i^c_{gd}\right)\\ u^c_{rqref}=\left(k_{pc}+k_{ic}/s\right)\left(i^c_{qref}-i^c_{gq}\right)+\omega_g L_g i^c_{gd}-K_C\left(i^c_q-i^c_{gq}\right)\end{cases},\tag{33}$$

where ω_g is the grid frequency; k_{pc} and k_{ic} represent the proportional and integral coefficients, respectively, of the inner current control loop; K_C is the proportionality coefficient of the capacitor current feedback.

Two state-space variables φ_d and φ_q are defined as follows:

$$\begin{cases}\dfrac{d\varphi_d}{dt}=i^c_{dref}-i^c_{gd}\\ \dfrac{d\varphi_q}{dt}=i^c_{qref}-i^c_{gq}\end{cases}.\tag{34}$$

Combining Eqs (5), (33) and (34), the linearised state-space model of the current loop can be given as follows:

$$\Delta\dot{x}_c=B_{c1}\Delta x_{PLL}+B_{c2}\Delta x_{LCL}+\Delta y_{PQ};\tag{35}$$

$$\Delta y_{cs}=C_c\Delta x_c+D_{c1}\Delta y_{dc}+D_{c2}\Delta x_{LCL}+D_{c4}\Delta x_{PLL},\tag{36}$$

where

$$\Delta x_c=\begin{bmatrix}\Delta\varphi_d & \Delta\varphi_q\end{bmatrix}^T;\tag{37}$$

$$\Delta y_{cs}=\begin{bmatrix}\Delta u^s_{rd} & \Delta u^s_{rq}\end{bmatrix}^T;\tag{38}$$

$$B_{c1}=\begin{bmatrix}0 & -I_{gd0}\\ 0 & I_{gq0}\end{bmatrix};\tag{39}$$

$$B_{c2}=\begin{bmatrix}0 & 0 & 0 & 0 & -1 & 0\\ 0 & 0 & 0 & 0 & 0 & -1\end{bmatrix};\tag{40}$$

$$C_c = \begin{bmatrix} k_{ic} & 0 \\ 0 & k_{ic} \end{bmatrix}; \tag{41}$$

$$D_{c1} = \begin{bmatrix} k_{pc} & 0 \\ 0 & k_{pc} \end{bmatrix}; \tag{42}$$

$$D_{c2} = \begin{bmatrix} -K_C & 0 & 0 & 0 & -k_{pc} + K_C & -\omega_g L_g \\ 0 & -K_C & 0 & 0 & \omega_g L_g & -k_{pc} + K_C \end{bmatrix}; \tag{43}$$

$$D_{c4} = \begin{bmatrix} 0 & \left(K_C - k_{pc}\right) I_{gq0} + \omega_g L_g I_{gd0} - K_C I_{q0} - U_{rq0} \\ 0 & \left(k_{pc} - K_C\right) I_{gd0} + \omega_g L_g I_{gq0} + K_C I_{d0} + U_{rd0} \end{bmatrix}. \tag{44}$$

Because of the sampling delay caused by digital control and the transmission delay caused by the digital pulse width modulation (PWM) unit (Wen et al., 2016), the delay unit needs to be added to the model, which can be given as follows:

$$\Delta \dot{x}_{del} = \begin{bmatrix} -\omega_d & 0 \\ 0 & -\omega_d \end{bmatrix} \Delta x_{del} + \begin{bmatrix} \omega_d & 0 \\ 0 & \omega_d \end{bmatrix} \Delta y_{cs} = A_{del} \Delta x_{del} + B_{del} \Delta y_{cs}; \tag{45}$$

$$\Delta y_{del} = \begin{bmatrix} 1 & 0 \\ 0 & 1 \end{bmatrix} \begin{bmatrix} \Delta u_d^s \\ \Delta u_q^s \end{bmatrix} = \Delta x_{del}, \tag{46}$$

where $\omega_d = 1/T_d$, and T_d is the total delay time of the system.

3.4. Electrical system model (power grid)

According to Kirchhoff's voltage law, the state-space model of the electrical system shown in Figure 2 can be expressed as shown in Eq. (47) (Wu et al., 2020):

$$\Delta \dot{x}_{LCL} = A_{LCL} \Delta x_{LCL} + B_{LCL1} \Delta y_{del} + B_{LCL2} \begin{bmatrix} \Delta u_{gd}^s \\ \Delta u_{gq}^s \end{bmatrix} + B_{LCL3} \Delta \omega, \tag{47}$$

where

$$A_{LCL} = \begin{bmatrix} 0 & \omega & -1/L_f & 0 & 0 & 0 \\ -\omega & 0 & 0 & -1/L_f & 0 & 0 \\ 1/C_f & 0 & 0 & \omega & -1/C_f & 0 \\ 0 & 1/C_f & -\omega & 0 & 0 & -1/C_f \\ 0 & 0 & 1/L_g & 0 & -R_g/L_g & \omega \\ 0 & 0 & 0 & 1/L_g & -\omega & -R_g/L_g \end{bmatrix}; \tag{48}$$

$$B_{LCL1} = \begin{bmatrix} 1/L_f & 0 & 0 & 0 & 0 & 0 \\ 0 & 1/L_f & 0 & 0 & 0 & 0 \end{bmatrix}^T; \tag{49}$$

$$B_{LCL2}=\begin{bmatrix}0 & 0 & 0 & 0 & -1/L_g & 0\\ 0 & 0 & 0 & 0 & 0 & -1/L_g\end{bmatrix}^T; \tag{50}$$

$$B_{LCL3}=\begin{bmatrix}I_{q0} & -I_{d0} & U_{pccq0} & -U_{pccd0} & I_{gq0} & -I_{gd0}\end{bmatrix}^T. \tag{51}$$

3.5. The state-space model of a GFL converter

Based on the above analysis, the state-space model of the GFL converter can be expressed as follows:

$$\Delta\dot{x}_{sys\_GFL}=A_{sys\_GFL}\Delta x_{sys\_GFL}+B_1\begin{bmatrix}\Delta u_{gd}^s\\ \Delta u_{gq}^s\end{bmatrix}+B_2\Delta\omega, \tag{52}$$

where Δx_{sys_GFL} is a 16×1 matrix, A_{sys_GFL} is a 16×16 matrix, B_1 is a 16×2 matrix, and B_2 is a 16×1 matrix.

$$\Delta x_{sys\_GFL}=\begin{bmatrix}\Delta x_{PLL} & \Delta x_{cal} & \Delta x_{PQ} & \Delta x_c & \Delta x_{del} & \Delta x_{LCL}\end{bmatrix}^T; \tag{53}$$

$$A_{sys\_GFL}=\begin{bmatrix}A_{PLL} & [0]_{2\times2} & [0]_{2\times2} & [0]_{2\times2} & [0]_{2\times2} & B_{PLL}\\ [0]_{2\times2} & A_{cal} & [0]_{2\times2} & [0]_{2\times2} & [0]_{2\times2} & B_{cal}\\ [0]_{2\times2} & B_{PQ1} & [0]_{2\times2} & [0]_{2\times2} & [0]_{2\times2} & [0]_{2\times6}\\ B_{c1} & D_{PQ} & C_{PQ} & [0]_{2\times2} & [0]_{2\times2} & B_{c2}\\ B_{del}D_{c4} & B_{del}D_{c1}D_{PQ} & B_{del}D_{c1}C_{PQ} & B_{del}C_c & A_{del} & B_{del}D_{c2}\\ [0]_{6\times2} & [0]_{6\times2} & [0]_{6\times2} & [0]_{6\times2} & B_{LCL1} & A_{LCL}\end{bmatrix}; \tag{54}$$

$$B_1=\begin{bmatrix}[0]_{10\times2}\\ B_{LCL2}\end{bmatrix}; \tag{55}$$

$$B_2=\begin{bmatrix}[0]_{10\times1}\\ B_{LCL3}\end{bmatrix}. \tag{56}$$

The SCR is usually defined to measure the strength of the power grid. According to the Institute of Electrical and Electronics Engineers (IEEE) Standard 1204-1997 (IEEE Std 1204-1997, 1997), when the SCR <2, the power grid is considered very weak. Alternatively, when the SCR >3, the power grid is considered strong. The definition of SCR can be expressed as follows:

$$SCR=\frac{S_{SC}}{S_N}=\frac{1.5{U_g}^2}{S_N Z_g}, \tag{57}$$

where S_{sc} is the short-circuit apparent power of the power grid; S_N is the rated apparent power of the inverter; U_g is the amplitude of the grid voltage; and Z_g is the amplitude of grid impedance.

In this paper, the SCR is changed by varying the values of the grid impedance Z_g. Long transmission lines will give large grid impedances and lead to a low SCR.

A simulation model of a 15-kW grid-connected converter is built in Matlab/Simulink and the key parameters of the case study system are listed in Table 2 (Gao et al., 2022).

According to the parameters listed in Table 2, the eigenvalue trajectory of the GFL converter can be plotted under various SCR values. When the SCR decreases from 7.5 to 1.0, the eigenvalue trajectory of the GFL converter is plotted in Figure 4. When the SCR decreases, the eigenvalues λ_1 and λ_2 move towards the right half plane, which means that the system loses stability. When the grid impedance is 20 mH and the corresponding SCR is 1.5, the system is in critical stability. When the grid impedance is >20 mH and the SCR is <1.5, the system becomes unstable.

Parameter	Description	Values
Grid		
U_g	Grid voltage	220 V
f_g	Grid frequency	50 Hz
L_g	Grid impedance	4–30 mH
R_g	Grid resistance	0.2–1.5 Ω
Converter		
u_{dc}	DC-link voltage	700 V
L_f	Impedance of LC filter	3 mH
C_f	Capacitance of LC filter	20 μF
P_{ref}	Reference of active power	15 kW
Q_{ref}	Reference of reactive power	0 kVar
f_s	Switching frequency	20 kHz
f_{sa}	Sampling frequency	20 kHz
Control parameters for the GFL converter		
ω_{pll}	Bandwidth of PLL	176 rad/s
ω_{PQ}	Bandwidth of power loop	78 rad/s
ω_i	Bandwidth of current loop	1,683 rad/s
K_C	P controller parameter of capacitor current feedback	15
ω_c	Cut-off frequency of low-pass filter	100 rad/s
Control parameters for the GFM converter		
ω_{vsg}	Bandwidth of VSG loop	14 rad/s
ω_u	Bandwidth of voltage loop	200 rad/s
ω_i	Bandwidth of current loop	1,683 rad/s
K_C	P controller parameter of capacitor current feedback	15
ω_c	Cut-off frequency of low-pass filter	100 rad/s
D	Damping coefficient	25
J	Virtual inertia	0.2 kg/m^2
k_u	Q-U loop coefficient	200
k_q	Integrity coefficient	0.1

GFL, grid-following; PLL, phase-locked loop; VSG, virtual synchronous generator.

Table 2. Parameters of a 15-kW grid-connected converter.

4. Control Structure of a GFM Converter

With the continuously increasing popularity of distributed renewable energy systems, the moment of inertia and damping of the entire power grid are decreasing. The stability of the power grid is at risk. Furthermore, the power of renewable energy systems injected into the distribution grid is dependent on the environmental conditions, which aggravates the instability of the power grid. In recent years, VSG control technology, which is one of the GFM control strategies, has attracted increasing attention because of its ability to imitate the inertia and damping characteristics of synchronous generators. Therefore, the power grid will have a strong ability to cope with the power fluctuations from the renewable energy systems and the load. Since this paper mainly focusses on grid-connected converters, to simplify the analysis, the DC side is just represented as an ideal DC source. The topology of a GFM converter with VSG control is shown in Figure 5, where E_m and θ represent the amplitude and phase angle of reference voltage, respectively.

4.1. VSG algorithm loop

The VSG algorithm is mainly composed of a power-frequency controller and an excitation controller. The power-frequency controller enables the converters to imitate the characteristics of synchronous generators. The excitation

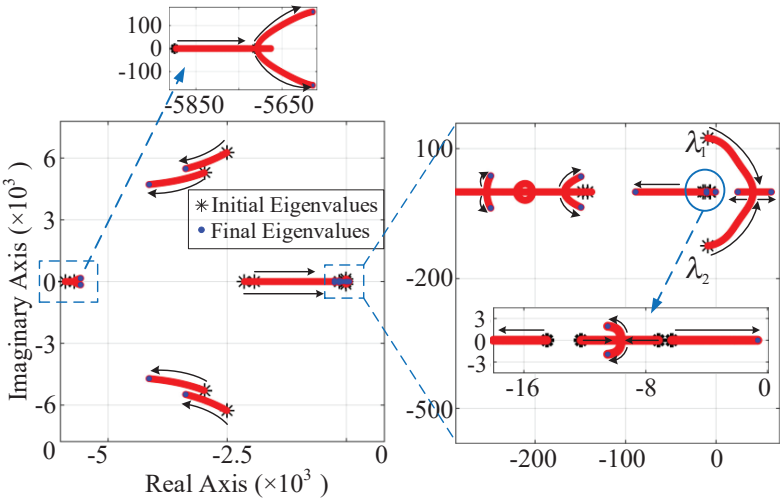

Fig. 4. Eigenvalue trajectory of the GFL converter with SCR changing from 7.5 to 1.0 and using the parameters in Table 2. GFL, grid-following; SCR, short-circuit ratio.

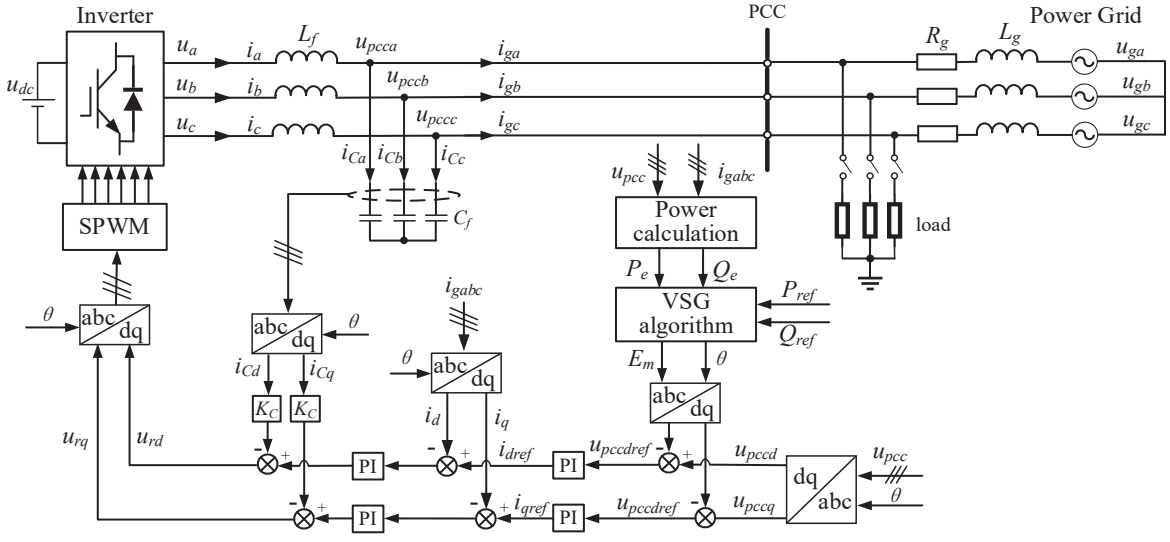

Fig. 5. The topology of a GFM converter with the VSG control. GFM, grid-forming; PCC, point of common coupling; PI, proportional integral; SPWM, sinusoidal pulse width modulation; VSG, virtual synchronous generators.

controller achieves the droop control between the voltage and the reactive power in the steady state. The two controllers can be given as follows (Peng et al., 2020; Zhong and Weiss, 2011):

$$\begin{cases} J\dfrac{d\omega}{dt} = \dfrac{P_{ref}}{\omega} - \dfrac{P_e}{\omega} - D\left(\omega - \omega_g\right) \\ \dfrac{d\theta}{dt} = \omega \end{cases}; \tag{58}$$

$$\frac{1}{k_q}\frac{dE_m}{dt} = Q_{ref} - Q_e + k_u\left(U_N - U_{pcc}\right), \tag{59}$$

where J is the moment of inertia; D is the damping coefficient; U_N is the rated voltage; U_{pcc} is the amplitude of the voltage at the PCC; k_q is the integrity coefficient; k_u is the voltage droop coefficient.

According to Eqs (58) and (59), the linearised small-signal model can be obtained and the state-space model of the VSG algorithm loop can be given as follows:

$$\Delta \dot{x}_{VSG} = A_{VSG}\Delta x_{VSG} + B_{VSG1}\Delta x_{cal} + B_{VSG2}\Delta x_{LCL}, \tag{60}$$

where

$$\Delta x_{VSG} = \begin{bmatrix} \Delta\omega & \Delta E_{dref} \end{bmatrix}^T; \tag{61}$$

$$A_{VSG} = \begin{bmatrix} -D/J & 0 \\ 0 & 0 \end{bmatrix}; \tag{62}$$

$$B_{VSG1} = \begin{bmatrix} -1/J\omega_g & 0 \\ 0 & -k_q \end{bmatrix}; \tag{63}$$

$$B_{VSG2} = \begin{bmatrix} 0 & 0 & 0 & 0 & 0 & 0 \\ 0 & 0 & -k_q k_u & 0 & 0 & 0 \end{bmatrix}. \tag{64}$$

4.2. Voltage control loop

The voltage control loop is used to regulate the voltages at the PCC to follow the references set by the VSG algorithm loop. The outputs of the voltage control loop are given as follows:

$$\begin{cases} i^c_{dref} = \left(k_{pu} + k_{iu}/s\right)\left(E_{dref} - u^c_{pccd}\right) - \omega_g C_f u^c_{pccq} \\ i^c_{qref} = \left(k_{pu} + k_{iu}/s\right)\left(0 - u^c_{pccq}\right) + \omega_g C_f u^c_{pccd} \end{cases}, \tag{65}$$

where k_{pu} and k_{iu} represent the proportional and integral coefficients, respectively, of the voltage control loop.

In order to express the equations simply, two state-space variables μ_d and μ_q are given as in Eq. (66):

$$\begin{cases} \dfrac{d\mu_d}{dt} = E_{dref} - u^c_{pccq} \\ \dfrac{d\mu_q}{dt} = -u^c_{pccq} \end{cases}. \tag{66}$$

Combining Eqs (65) and (66), the state-space model of the voltage loop can be expressed as follows:

$$\Delta \dot{x}_u = B_{u1}\Delta x_{VSG} + B_{u2}\Delta x_{LCL}; \tag{67}$$

$$\Delta y_u = C_u \Delta x_u + D_{u1}\Delta x_{VSG} + D_{u2}\Delta x_{LCL}, \tag{68}$$

where

$$\Delta x_u = \begin{bmatrix} \Delta\mu_d & \Delta\mu_q \end{bmatrix}^T; \tag{69}$$

$$\Delta y_u = \begin{bmatrix} \Delta i^c_{dref} & \Delta i^c_{qref} \end{bmatrix}^T; \tag{70}$$

$$B_{u1}=\begin{bmatrix}0 & 1\\ 0 & 0\end{bmatrix}; \tag{71}$$

$$B_{u2}=\begin{bmatrix}0 & 0 & -1 & 0 & 0 & 0\\ 0 & 0 & 0 & -1 & 0 & 0\end{bmatrix}; \tag{72}$$

$$C_u=\begin{bmatrix}k_{iu} & 0\\ 0 & k_{iu}\end{bmatrix}; \tag{73}$$

$$D_{u1}=\begin{bmatrix}0 & k_{pu}\\ 0 & 0\end{bmatrix}; \tag{74}$$

$$D_{u2}=\begin{bmatrix}0 & 0 & -k_{pu} & -\omega_g C_f & 0 & 0\\ 0 & 0 & \omega_g C_f & -k_{pu} & 0 & 0\end{bmatrix}. \tag{75}$$

4.3. Current control loop

The current control loop of the GFM control is the same as that of the GFL control, so it will not be described here again. The state-space model of the current control loop can be expressed as follows:

$$\Delta \dot{x}_c = B_{c2}\Delta x_{LCL} + \Delta y_u ; \tag{76}$$

$$\Delta y_c = C_c\Delta x_c + D_{c1}\Delta y_u + D_{c2}\Delta x_{LCL} ; \tag{77}$$

$$\Delta \dot{x}_{del} = A_{del}\Delta x_{del} + B_{del}\Delta y_c . \tag{78}$$

4.4. Electrical system model (power grid)

The electrical system model of the GFM converter is similar to that of the GFL converter, which is illustrated in Section 3. However, the value of $\Delta\omega$ is obtained from the VSG algorithm loop. The state-space model of the electrical system can be given as in Eq. (79):

$$\Delta \dot{x}_{LCL} = A_{LCL}\Delta x_{LCL} + B_{LCL1}\Delta y_{del} + B_{LCL2}\begin{bmatrix}\Delta u_{gd}^s\\ \Delta u_{gq}^s\end{bmatrix} + B_{LCL4}\Delta x_{VSG} , \tag{79}$$

where B_{LCL4} is a 16×2 matrix:

$$B_{LCL4}=\begin{bmatrix}B_{LCL3} & [0]_{6\times 1}\end{bmatrix}. \tag{80}$$

4.5. The state-space model of a GFM converter

Based on the above analysis, the state-space model of the GFM converter can be expressed as follows:

$$\Delta \dot{x}_{sys\_GFM} = A_{sys\_GFM}\Delta x_{sys\_GFM} + B_1\begin{bmatrix}\Delta u_{gd}^s\\ \Delta u_{gq}^s\end{bmatrix}, \tag{81}$$

where Δx_{sys_GFM} is a 16×1 matrix, A_{sys_GFM} is a 16×16 matrix.

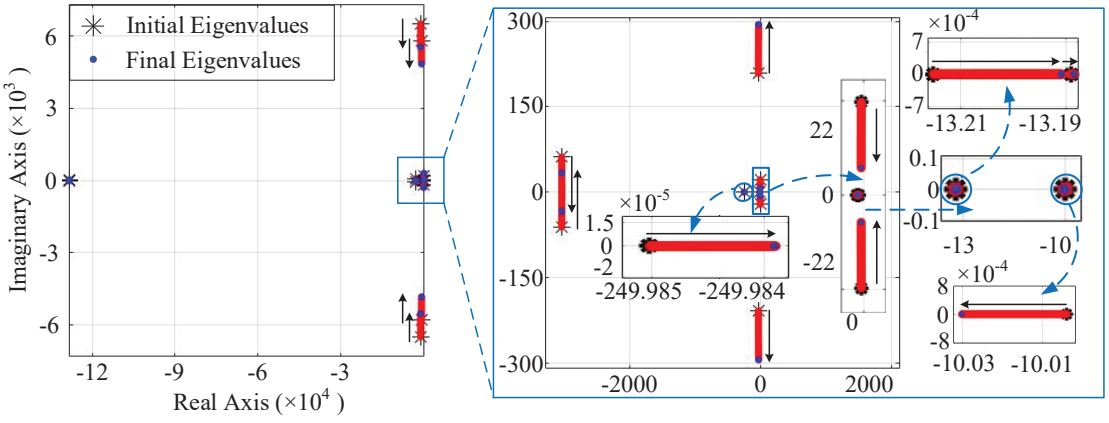

Fig. 6. Eigenvalue trajectory of the GFM converter with SCR changing from 7.5 to 1.0 and using the parameters in Table 2. GFM, grid-forming; SCR, short-circuit ratio.

$$\Delta x_{sys\_GFM} = \begin{bmatrix} \Delta x_{cal} & \Delta x_{VSG} & \Delta x_u & \Delta x_c & \Delta x_{del} & \Delta x_{LCL} \end{bmatrix}^T; \tag{82}$$

$$A_{sys\_GFM} = \begin{bmatrix} A_{cal} & [0]_{2\times2} & [0]_{2\times2} & [0]_{2\times2} & [0]_{2\times2} & B_{cal} \\ B_{VSG1} & A_{VSG} & [0]_{2\times2} & [0]_{2\times2} & [0]_{2\times2} & B_{VSG2} \\ [0]_{2\times2} & B_{u1} & [0]_{2\times2} & [0]_{2\times2} & [0]_{2\times2} & B_{u2} \\ [0]_{2\times2} & D_{u1} & C_u & [0]_{2\times2} & [0]_{2\times2} & B_{c2}+D_{u2} \\ [0]_{2\times2} & B_{del}D_{c1}D_{u1} & B_{del}D_{c1}C_u & B_{del}C_c & A_{del} & B_{del}D_{c2}+B_{del}D_{c1}D_{u2} \\ [0]_{6\times2} & B_{LCL4} & [0]_{6\times2} & [0]_{6\times2} & B_{LCL1} & A_{LCL} \end{bmatrix}. \tag{83}$$

According to the parameters shown in Table 2 in Section 3, the eigenvalue trajectory of the GFM converter can be plotted. In Figure 6, the eigenvalue trajectory of the GFM converter is plotted when the grid impedance increases from 4 mH to 30 mH and the corresponding SCR decreases from 7.5 to 1.0. It can be seen that when the SCR decreases, all the eigenvalues are still in the left half plane, which means that the system stays stable.

5. Simulation Results: Case Study

In order to demonstrate the aforementioned control schemes, a simulation model of 15 kW grid-connected converter is built in Matlab/Simulink. The SCR of the case study is 7.5. The parameters are shown in Table 2 in Section 3. The case of loss of generation and load shed are chosen to compare the different performances of the GFL and GFM controls. In order to discuss the different dynamic responses of the GFL and GFM controls under operation at different SCRs, a simulation is carried out in the case of load increase.

According to the IEEE 1547-2018 standard (IEEE Std 1547-2018, 2018), the rated frequency is 60.0 Hz and the normal operating range of the system frequency is from 58.8 Hz to 62.0 Hz. Converting to the per-unit (pu) values, the normal operating deviation of the frequency is from -0.02 pu to + 0.03 pu. Furthermore, the rate of change of frequency (RoCoF) is limited to 3.0 Hz/s. Therefore, in this case study, the normal frequency range is from 48.3 Hz to 51.5 Hz and the RoCoF is limited to 2.5 Hz/s.

5.1. Performance under loss of generation

During the period spanning 2–3 s, the loss of generation happens. The reference and feedback of output active power, reactive power and grid currents, as well as the output voltages under the *d-q* axis for the GFL control, are shown in Figure 7. It can be seen that both the outer power loop and inner current loop can work well.

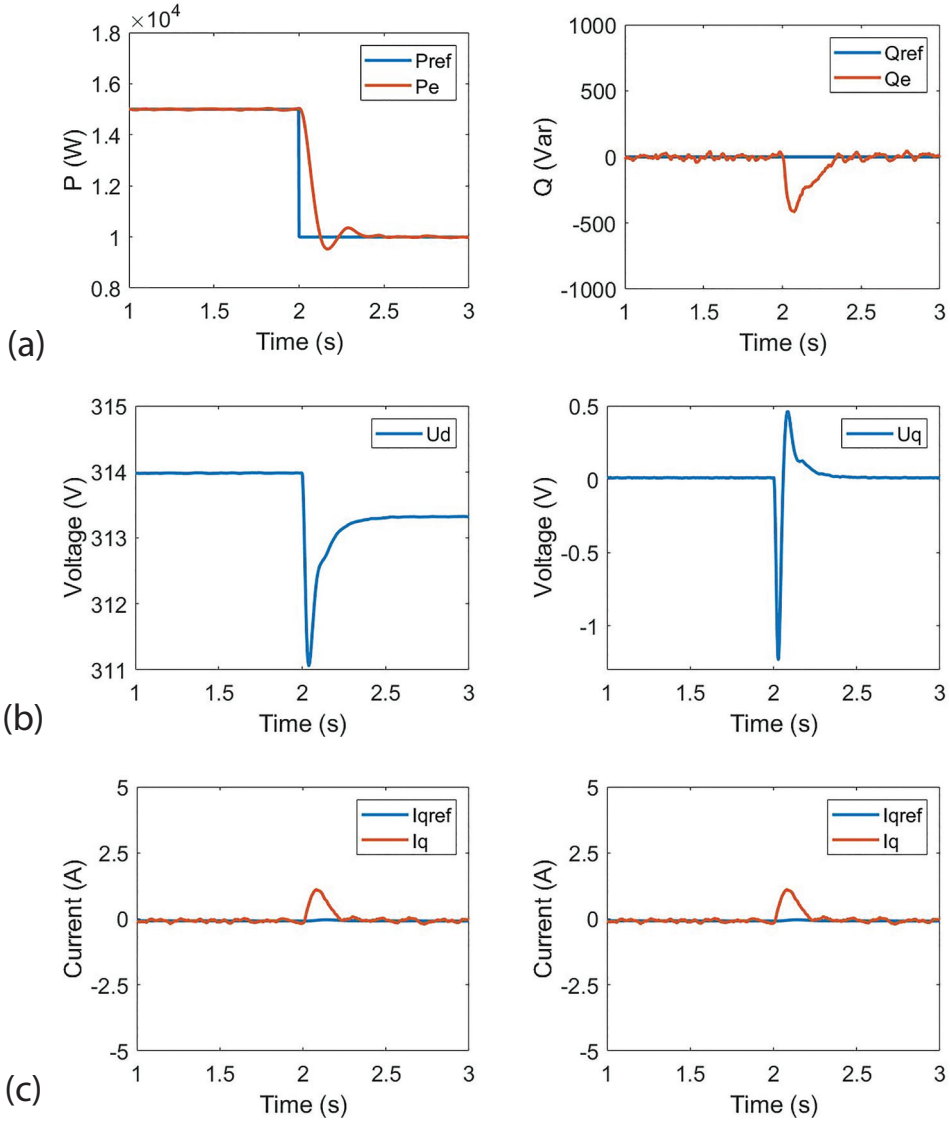

Fig. 7. Controllers of the GFL converter under loss of generation: (a) Outer power loop; (b) output voltages; (c) inner current loop. GFL, grid-following.

According to the definition of the complex power, the active power P_e and the reactive power Q_e flowing between the PCC and the power grid can be expressed as follows:

$$\begin{cases} P_e = \dfrac{3U_{pcc}{}^2 \cos\alpha - 3U_{pcc}U_g \cos(\alpha+\delta)}{Z_g} \\ Q_e = \dfrac{3U_{pcc}{}^2 \sin\alpha - 3U_{pcc}U_g \sin(\alpha+\delta)}{Z_g} \end{cases}, \tag{84}$$

where δ is the phase angle difference between the PCC voltage and the grid voltage; α represents the angle of the grid impedance.

The relationship between the P_e, Q_e *and* U_{pcc} satisfies the equation given as follows:

$$U_{pcc} = \frac{1}{2}U_g + \frac{\sqrt{9U_g{}^2 + 12(P_eR_g + Q_eX_g)}}{6}. \tag{85}$$

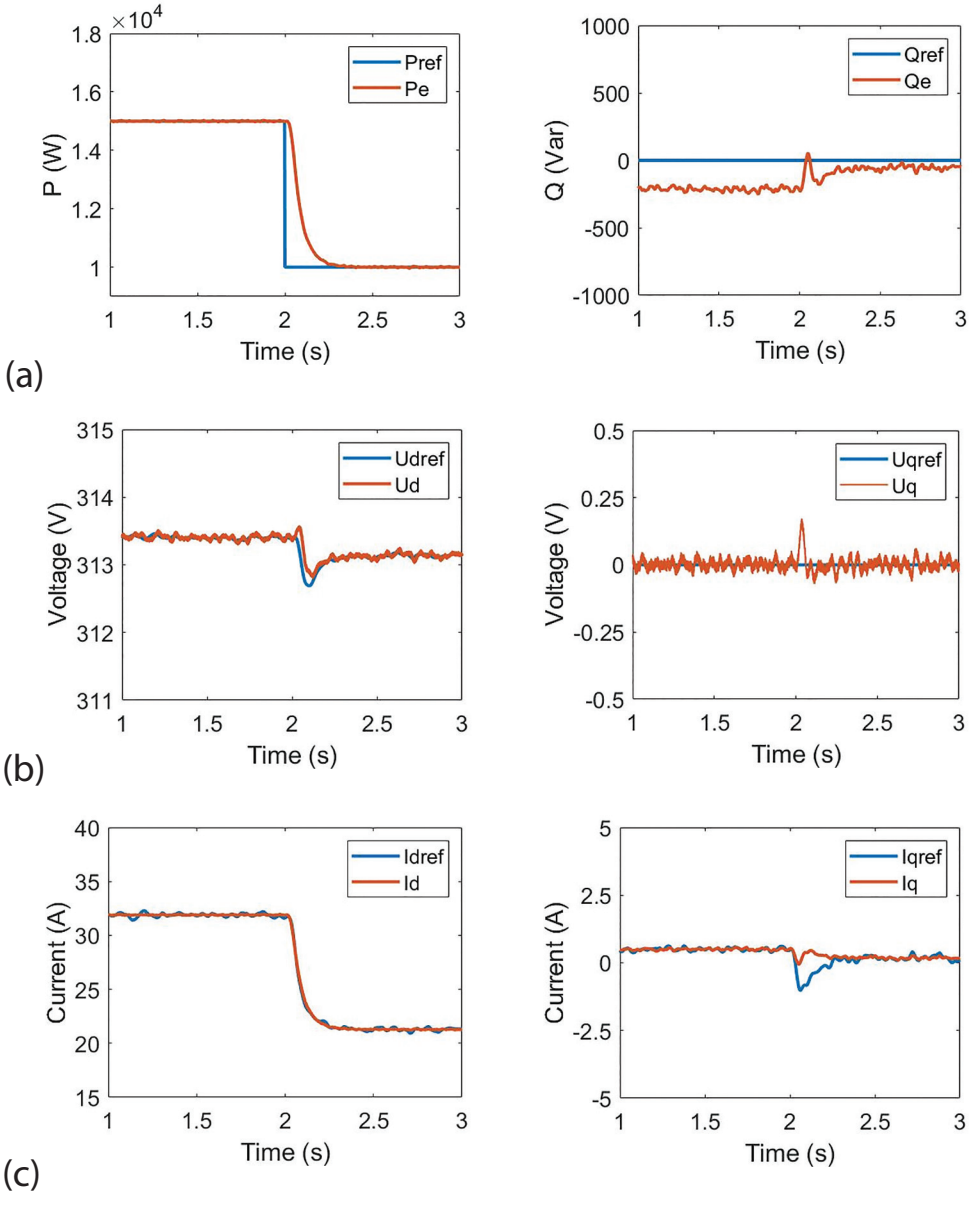

Fig. 8. Controllers of the GFM converter under loss of generation: (a) VSG algorithm; (b) voltage loop; (c) inner current loop. GFM, grid-forming; VSG, virtual synchronous generators.

Because of the existence of grid impedance and because the resistance–inductance ratio of grid impedance is not low enough in this case study, the change of the active power will lead to the change of PCC voltage. When the active power decreases, the voltage at the PCC will decrease accordingly, which is shown in Figure 7b.

Similarly, the reference and feedback of active power and reactive power, the output voltages and the grid currents under the d-q axis for the GFM control are shown in Figure 8. All the control loops can work well. It is worth mentioning that because of the droop relationship between Qe and Upcc, there is a difference between Qe and Qref in the steady state, which is shown in Figure 8a.

The simulation results of the converter output power, frequency and RoCoF at the PCC are shown in Figure 9. It is worth noting that for both the GFL control and GFM control, the frequency and the RoCoF are measured from the PLL unit. However, for the GFM control, the PLL unit is just used for the measurement, and the frequency used for the control is from the VSG algorithm loop. Compared with the GFL control, the GFM control can slow down the changes of the converter output, reflecting the inertial response characteristics. In addition, a higher frequency

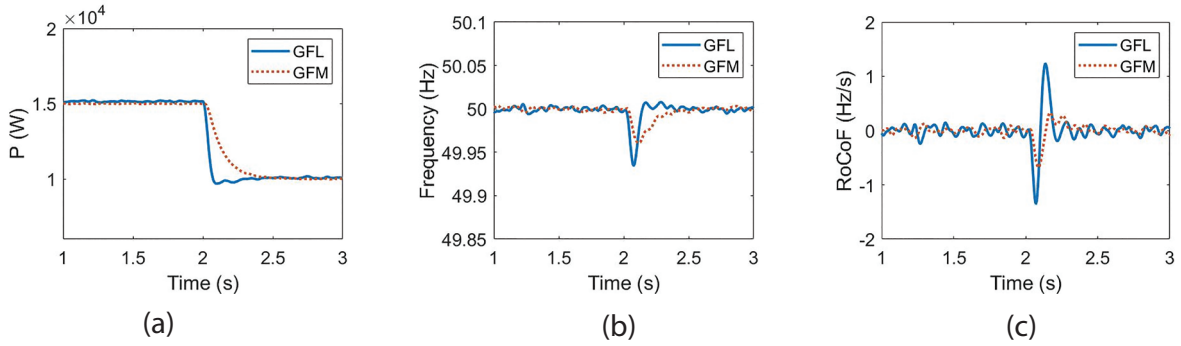

Fig. 9. Simulation results under loss of generation: (a) Converter output power; (b) frequency at the PCC; (c) RoCoF at the PCC. GFL, grid-following; GFM, grid-forming; PCC, point of common coupling; RoCoF, rate of change of frequency.

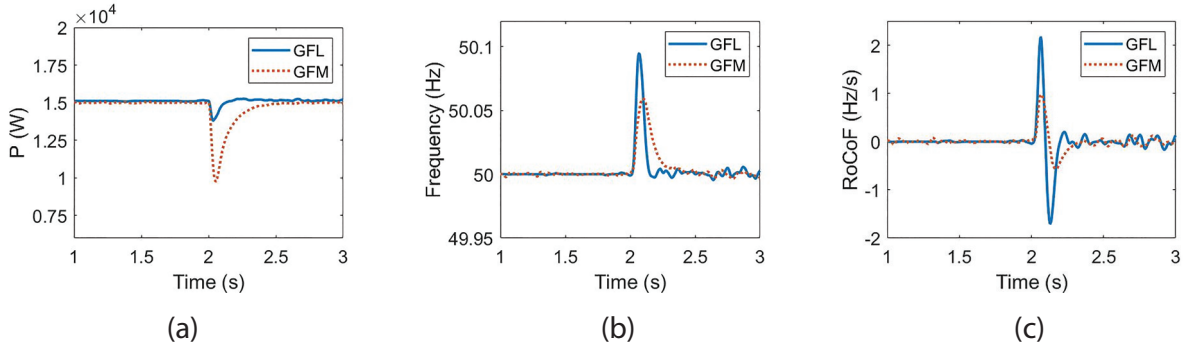

Fig. 10. Simulation results under a sudden load shed: (a) Converter output power; (b) frequency at the PCC; (c) RoCoF at the PCC. GFL, grid-following; GFM, grid-forming; PCC, point of common coupling; RoCoF, rate of change of frequency.

nadir and a lower RoCoF can be provided by the GFM control, which improves the stability of the power grid during sudden changes of generation and facilitates a strong ability to cope with the fluctuations of renewable energy generation.

5.2. Performance under a sudden load shed

During the period spanning 2–3 s, a sudden load shed is applied to the power grid. The simulation results of the converter output power, frequency and RoCoF at the PCC are shown in Figure 10. Compared with the GFL control, the GFM control avoids the sudden increase in frequency, which enhances the ability of the power grid to handle the case of load fluctuations. As shown in Figures 10b and 10c, with the GFM control, both the frequency culmination and the RoCoF decrease significantly.

5.3. Performance under operation at different SCRs

The simulation results of frequency and RoCoF at the PCC in the case of operation at different SCRs are shown in Figures 11 and 12, respectively. During the period spanning 2–3 s, a load step is applied to the power grid. As shown in Figures 11 and 12, whether with GFL control or GFM control, the impact of load step on the power grid is large when the value of SCR is small. In addition, with the GFM control, the frequency nadir is increased and the RoCoF is decreased, which reduces the influence of sudden load increase and enhances the stability of the power grid. When the SCR is equal to '1', the GFL control cannot maintain stable operation, while the GFM control still works well. Although the value of RoCoF is beyond the limits of the IEEE 1547-2018 standard (IEEE Std 1547-2018, 2018), it can be solved by regulating the virtual inertia and damping coefficient. The simulation results are consistent with the theoretical analysis in Sections 3 and 4. The GFL converter may encounter some instability

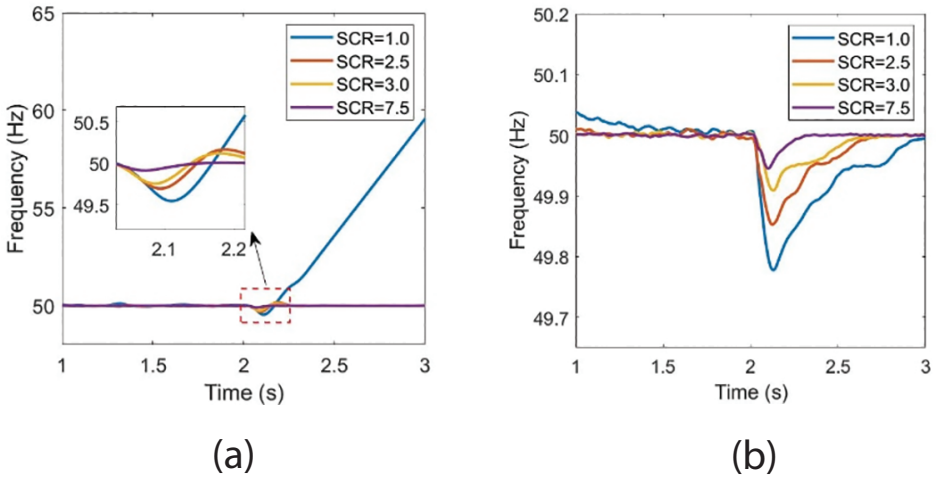

Fig. 11. Simulation results of frequency at the PCC under operation at different SCRs: (a) GFL converter (b) GFM converter. GFL, grid-following; GFM, grid-forming; PCC, point of common coupling; SCR, short-circuit ratio.

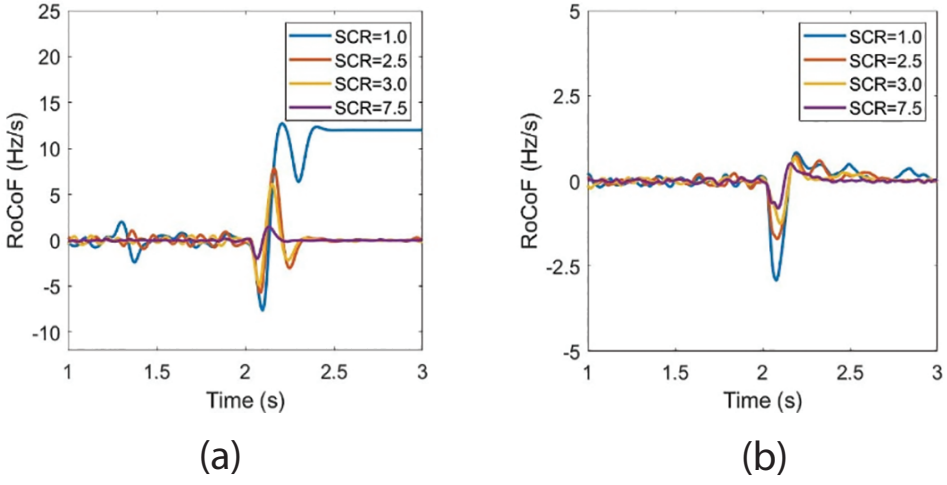

Fig. 12. Simulation results of RoCoF at the PCC under operation at different SCRs: (a) GFL converter; (b) GFM converter. GFL, grid-following; GFM, grid-forming; PCC, point of common coupling; RoCoF, rate of change of frequency; SCR, short-circuit ratio.

issues when applied in a weak power grid, while the GFM converter is more suitable for operation with a weak power grid.

6. Conclusion

This paper analysed the control schemes of GFL converters and GFM converters. The state-space models of both the GFL converters and GFM converters were built. Through a case study, the dynamic responses of GFL control and GFM control under various working conditions were compared. The grid-connected converter with the GFM control was shown to be able to slow down the change of converter output, reflecting the inertial response characteristics of conventional synchronous generators, and to improve the grid's ability to cope with sudden frequency disturbances, i.e., fluctuations of generation and load. Analysis of the simulation results showed that the smaller the SCR becomes, the larger is the influence that frequency disturbances have on the power grid. Furthermore, compared with the GFL converter, the GFM converter is more suitable for a weak power grid.

References

Adapa, A. K. and John, V. (2018). Virtual resistor based active damping of LC filter in standalone voltage source inverter. In: *Proceedings of APEC 2018*, USA, 4-8 Mar. 2018, pp. 1834–1840.

Chen, M., Zhou, D. and Blaabjerg, F. (2020). Modelling, Implementation, and Assessment of Virtual Synchronous Generator in Power Systems. *Journal of Modern Power Systems and Clean Energy,* 8(3), pp. 399–411.

Dahono, P. A., Bahar, Y. R., Sato, Y. and Kataoka, T. (2001). Damping of transient oscillations on the output LC filter of PWM inverters by using a virtual resistor. In: *Proceedings of 4th IEEE International Conference on Power Electronics and Drive Systems*, Denpasar, Indonesia, 25 Oct. 2018, pp. 403–407.

Dong, D., Wen, B., Boroyevich, D., Mattavelli, P. and Xue, Y. (2015). Analysis of Phase-Locked Loop Low-Frequency Stability in Three-Phase Grid-Connected Power Converters Considering Impedance Interactions. *IEEE Transactions on Industrial Electronics,* 62(1), pp. 310–321.

Du, W., Tuffner, F., Schneider, K. P., Lasseter, R. H., Xie, J., Chen, Z. and Bhattarai, B. P. (2020). Modeling of Grid-Forming and Grid-Following Inverters for Dynamic Simulation of Large-Scale Distribution Systems. *IEEE Transactions on Power Delivery,* 36(4), pp. 2035–2045.

Fang, J., Li, H., Tang, Y. and Blaabjerg, F. (2018). Distributed Power System Virtual Inertia Implemented by Grid-Connected Power Converters. *IEEE Transactions on Power Electronics,* 33(10), pp. 8488–8499.

Gao, X., Zhou, D., Anvari-Moghaddam, A. and Blaabjerg, F. (2021). Grid-following and grid-forming control in power electronic based power systems: A comparative study. In: *Proceedings of IECON 2021 – 47th Annual Conference of the IEEE Industrial Electronics Society*, Toronto, 13-16 Oct. 2021, pp. 1–6.

Gao, X., Zhou, D., Anvari-Moghaddam, A. and Blaabjerg, F. (2022). Stability analysis of grid-following and grid-forming converters based on state-space model. *In: Proceedings of 2022 International Power Electronics Conference (IPEC-Himeji 2022-ECCE Asia)*, Himeji, 15-19 May 2022, pp. 422–428.

IEEE Guide for Planning DC Links Terminating at AC Locations Having Low Short-Circuit Capacities. (1997). IEEE Standard 1204-1997, 1997, pp. 1-216.

IEEE Standard for Interconnection and Interoperability of Distributed Energy Resources with Associated Electric Power Systems Interfaces. (2018). IEEE Standard 1547-2018 (Revision of IEEE Standard 1547-2003), 2018, pp. 1-138.

Lasseter, R. H., Chen, Z. and Pattabiraman, D. (2020). Grid-Forming Inverters: A Critical Asset for the Power Grid. *IEEE Journal of Emerging and Selected Topics in Power Electronics,* 8(2), pp. 925–935.

Pattabiraman, D., Lasseter, R. H. and Jahns, T. M. (2018). Comparison of grid following and grid forming control for a high inverter penetration power system. *In: Proceedings of 2018 IEEE Power* and *Energy Society General Meeting PESGM*, Portland or USA, 5-10 Aug. 2018, pp. 1–5.

Peng, Q., Jiang, Q., Yang, Y., Liu, T., Wang, H. and Blaabjerg, F. (2019). On the Stability of Power Electronics-Dominated Systems: Challenges and Potential Solutions. *IEEE Transactions on Industry Applications,* 55(6), pp. 7657–7670.

Peng, Q., Yang, Y., Liu, T. and Blaabjerg, F. (2020). Coordination of Virtual Inertia Control and Frequency Damping in PV Systems for Optimal Frequency Support. *CPSS Transactions on Power Electronics and Applications,* 5(4), pp. 305–316.

Rocabert, J., Luna, A., Blaabjerg, F. and Rodríguez, P. (2012). Control of Power Converters in AC Microgrids. *IEEE Transactions on Power Electronics,* 27(11), pp. 4734–4749.

Rosso, R., Wang, X., Liserre, M., Lu, X. and Engelken, S. (2021). Grid-Forming Converters: Control Approaches, Grid-Synchronization, and Future Trends – A Review. *IEEE Open Journal of Industry Applications,* 2, pp. 93–109.

Sangwongwanich, A., Abdelhakim, A., Yang, Y. and Zhou, K. (2018). Control of single-phase and three-phase DC/AC converters. In: F. Blaabjerg, ed., *Control of Power Electronic Converters and Systems*. Academic Press, Amsterdam, The Netherlands, pp. 153–173.

Wang, X., Taul, M. G., Wu, H., Liao, Y., Blaabjerg, F. and Harnefors, L. (2020). Grid-Synchronization Stability of Converter-Based Resources – An Overview. *IEEE Open Journal of Industry Applications,* 1, pp. 115–134.

Wen, B., Boroyevich, D., Burgos, R., Mattavelli, P. and Shen, Z. (2016). Analysis of D-Q Small-Signal Impedance of Grid-Tied Inverters. *IEEE Transactions on Power Electronics,* 31(1), pp. 675–687.

Wu, G., Sun, H., Zhang, X., Egea-Alvarez, A., Zhao, B., Xu, S., Wang, S. and Zhou, X. (2020). Parameter Design Oriented Analysis of the Current Control Stability of the Weak-Grid-Tied VSC. *IEEE Transactions on Power Delivery,* 36(3), pp. 1458–1470.

Xie, Z., Chen, Y., Wu, W., Xu, Y., Wang, H., Guo, J. and Luo, A. (2019). Modeling and Control Parameters Design for Grid-Connected Inverter System Considering the Effect of PLL and Grid Impedance. *IEEE Access,* 8, pp. 40474–40484.

Yang, L., Chen, Y., Luo, A., Chen, Z., Zhou, L., Zhou, X., Wu, W., Tan, W. and Guerrero, J. M. (2019). Effect of Phase-Locked Loop On Small-Signal Perturbation Modelling and Stability Analysis for Three-Phase LCL-Type Inverter Connected to Weak Grid. *IET Renewable Power Generation,* 13(7), pp. 86–93.

Zhong, Q. and Weiss, G. (2011). Synchronverters: Inverters That Mimic Synchronous Generators. *IEEE Transactions on Industrial Electronics,* 58(4), pp. 1259–1267.